HAL
open science

Understanding Grain Boundary Electrical Resistivity in Cu: The Effect of Boundary Structure

Hanna Bishara, Subin Lee, Tobias Brink, Matteo Ghidelli, Gerhard Dehm

To cite this version:

Hanna Bishara, Subin Lee, Tobias Brink, Matteo Ghidelli, Gerhard Dehm. Understanding Grain Boundary Electrical Resistivity in Cu: The Effect of Boundary Structure. ACS Nano, 2021, 15 (10), pp.16607 - 16615. 10.1021/acsnano.1c06367 . hal-03424007

HAL Id: hal-03424007

https://hal.science/hal-03424007v1

Submitted on 10 Nov 2021

HAL is a multi-disciplinary open access archive for the deposit and dissemination of scientific research documents, whether they are published or not. The documents may come from teaching and research institutions in France or abroad, or from public or private research centers.

L'archive ouverte pluridisciplinaire **HAL**, est destinée au dépôt et à la diffusion de documents scientifiques de niveau recherche, publiés ou non, émanant des établissements d'enseignement et de recherche français ou étrangers, des laboratoires publics ou privés.

ACSNANO

www.acsnano.org

Understanding Grain Boundary Electrical Resistivity in Cu: The Effect of Boundary Structure

Hanna Bishara,* Subin Lee, Tobias Brink, Matteo Ghidelli, and Gerhard Dehm*

Cite This: *ACS Nano* 2021, 15, 16607−16615

Read Online

ACCESS | Metrics & More | Article Recommendations | Supporting Information

ABSTRACT: **Grain boundaries (GBs) in metals usually increase electrical resistivity due to their distinct atomic arrangement compared to the grain interior. While the GB structure has a crucial influence on the electrical properties, its relationship with resistivity is poorly understood. Here, we perform a systematic study on the resistivity−structure relationship in Cu tilt GBs, employing high-resolution *in situ* electrical measurements coupled with atomic structure analysis of the GBs. Excess volume and energies of selected GBs are calculated using molecular dynamics simulations. We find a consistent relation between the coincidence site lattice (CSL) type of the GB and its resistivity. The most resistive GBs are in the high range of low-angle GBs (14°−18°) with twice the resistivity of high angle tilt GBs, due to the high dislocation density and corresponding strain fields. Regarding the atomistic structure, GB resistivity approximately correlates with the GB excess volume. Moreover, we show that GB curvature increases resistivity by ∼80%, while phase variations and defects within the same CSL type do not considerably change it.**

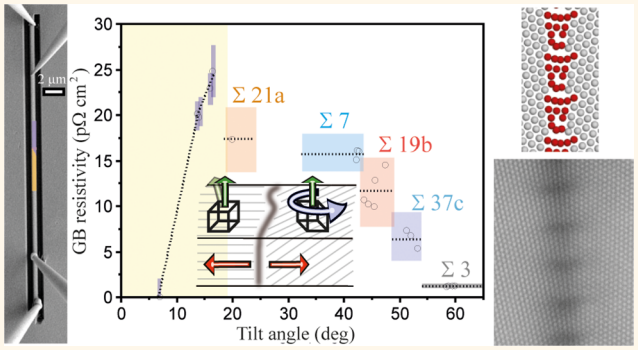

KEYWORDS: *grain boundaries, electrical resistivity, grain boundary structure, copper, excess volume*

INTRODUCTION

The electrical resistivity of grain boundaries (GBs) in conductive materials hampers the development of nano-electronic and energy-harvesting devices. For instance, GB resistivity is a major concern for electron transport in sub-20 nm interconnects in integrated circuits,[1−5] while GBs in thermoelectric and photovoltaic materials are suspected to decrease device efficiency.[6,7] To overcome these challenges, GB engineering has been utilized to optimize the material's functional performance, for example, through a controlled sample preparation or processing.[8−10] In doing so, the scientific community relies on experimental evidence that GB resistivity is decreased for low-angle GBs (LAGBs) and twin boundaries.[3,8,9,11,12] Nevertheless, experimental studies on the impact of GB characteristics, such as, type, misorientation or inclination, phase, and curvature on resistivity are still missing due to limitations of the spatial resolution and sensitivity of resistivity measurements.

The relationship between the resistivity of a GB and its structural characteristics arises from the altered atomic structure of the GB compared to the grain interior. This creates a fluctuation in the periodic atomic potential from the adjacent crystals across the boundary, leading to electron scattering at the boundary by a potential wall. The magnitude of the potential wall is associated with the GB structure and its chemical bonding.[13,14] Moreover, the distinct atomic arrangements at the GB also locally change the density of states and electron density compared to the grain interior[15] as confirmed by density functional theory (DFT) simulations.[12,14,16] However, its experimental observation is challenging because of the difficulties in isolating a specific GB and characterizing solely its resistivity.[13,17,18] Hence, cumulative scattering events on the different GBs blur out all details of the influence of GB type and character on resistivity. To overcome this challenge, there is a need to probe the electrical resistivity of an individual GB segment. Nakamichi[19] inspected individual GBs in bulk bicrystals and experimentally revealed a misorientation dependence of the resistivity. However, this study, which was

Received: July 27, 2021
Accepted: September 28, 2021
Published: October 4, 2021

Downloaded via UNIV PARIS 13 on November 10, 2021 at 10:33:23 (UTC).
See https://pubs.acs.org/sharingguidelines for options on how to legitimately share published articles.

ACS Publications

© 2021 The Authors. Published by American Chemical Society

https://doi.org/10.1021/acsnano.1c06367
ACS Nano 2021, 15, 16607−16615

conducted at cryogenic temperature, did not consider the GB characteristics, for example, its inclination, phases, curvature, or defects. Later, small-scale approaches were introduced to locally probe single, submicrometer GB segments using micromanipulators.[20−22] Recently, we further improved this method to gain ultrahigh sensitivity, enabling resistivity measurements of a Σ3 Cu GB.[23] Here, we adopt this technique and extend the research to a systematic study of the effect of different individual GB structures on resistivity in a polycrystalline Cu thin film with [111] tilt GBs.

Within the context of tilt GBs, the geometric relation between neighboring grains is described through the tilt axis, misorientation angle θ, and the normal(s) of the GB plane(s) in each case. For symmetric GBs, a common plane exists, while for an asymmetric boundary the GB plane normals are different in the adjacent grains. For discrete tilt angles θ_{CSL}, corresponding to coincidence site lattices (CSLs), GBs exhibit specific periodic atomic structures (motifs).[24] The same motifs prevail for GBs even at some deviations of $\delta\theta$ from the exact θ_{CSL} within the Brandon criterion (maximum angle of deviation from an exact CSL that could be sustained by a dislocation array).[25] The atomic configurations of GBs can be predicted by atomistic simulations and resolved through the aberration-corrected (scanning) transmission electron microscopy ((S)TEM) imaging.[26−28] The equilibrium structure of the GB in a pure material depends not only on the misorientation between the neighboring grains and the GB plane, but also on temperature and pressure conditions. Analogous to bulk phases, the resulting structures are referred to as GB phases.[26,29,30] For metals, it has only recently been observed that a specific GB can have different phases[26,31] as predicted earlier by interface thermodynamics.[29,30,32] In terms of interface thermodynamics, GB phases are described by their excess interfacial energy E_{gb}, excess volume ΔV, excess entropy, and interface stress.[32] These thermodynamic state variables determine the GB phase stability, while kinetics control the transformation velocities. In recent studies, three GB phases were observed for Cu Σ19b GBs via atomic-scale STEM and by molecular dynamics (MD) computer simulations.[31,33] In some cases, different GB phases were found in the same GB segment.

In this context, this study focuses on Cu, on the one hand, as a model system that has been investigated with respect to different GB structures, and on the other hand, due to the high application relevance concerning its electronic properties for integrated circuits. We consider different Cu [111] tilt GBs, namely Σ3, Σ7, Σ19b, Σ21a, and Σ37c, as well as LAGBs with misorientation angles ranging from 7° to 18°. The study sheds light on similarities and differences in GB resistivity for (i) symmetric and asymmetric variants, (ii) variations in GB inclination, (iii) deviations from the ideal CSL, (iv) introduction of twist components, (v) macroscopic curvature, and (vi) possible different GB phases (see Figure 1).

RESULTS AND DISCUSSION

Selection of Different Grain Boundaries. Well-defined tilt GBs in Cu are achieved through the deposition of a thin film by magnetron sputtering on a c-plane α-Al_2O_3 (sapphire) surface, as this is known to create [111] tilt GBs aligned vertical to the surface.[34,35] The electron backscatter diffraction (EBSD)-resolved inverse pole figure maps, shown in Figure 2a,b, confirm an abnormal grain growth and uniform (111) planes parallel to the surface. The abnormal grain growth

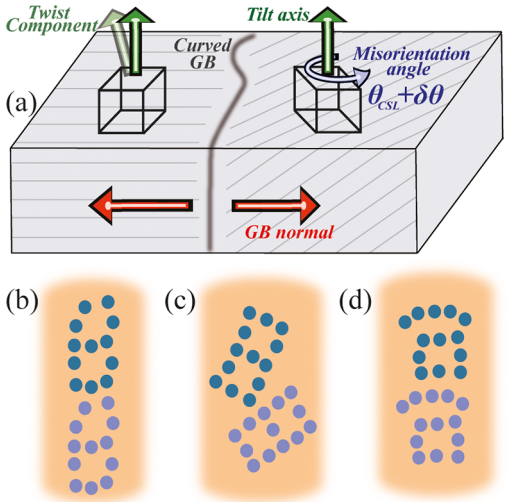

Figure 1. (a) Parameters to describe the relative crystallographic orientation between adjacent grains. The <111> tilt axis is indicated by green arrows. An inclination of this tilt axis leads to a twist component within the GB. GB plane normals are represented by red arrows. The resulting misorientation between the grains ($\theta_{CSL}+\delta\theta$) determines the CSL value, with the deviation from the exact CSL angle denoted as $\delta\theta$. Finally, GBs might be straight or curved macroscopically. For Σ19b GBs (θ = 46.8°), three possible GB phases occur with different atomic arrangements:[31,33] (b) zipper for the symmetric (23$\bar{5}$) GB plane, as well as (c) domino and (d) pearl for the symmetric (1$\bar{8}$7) GB plane. The atomic arrangements are shown here in the projection from the <111> direction.

indicates the high purity of the Cu film, otherwise GB segregation could occur which can cause GB pinning and growth stagnation at smaller grain sizes. The room temperature deposition yields alignment of the (111) plane in Cu parallel to the (0001) sapphire planes, while Cu might get random in-plane orientations.[34−36] Upon annealing, the microstructure evolves with grain growth with several tilt GB types. The driving force for the abnormal grain growth mechanism is not fully understood yet, since it is affected by several factors, for example, local curvature of GBs, mobility of triple points, surface steps of the substrate, and misorientation-dependent in-plane coherency stress.[37−39]

The subtly different blue colors in Figure 2a indicate a small twist component between some of the grains up to 3°. The (111) pole figure in Figure 2c implies two ranges of misorientation angles: below ∼21°, and between 42° and 60°. The majority of the GBs are Σ3 boundaries, and there are CSL boundaries also, for example Σ7, Σ19b, Σ21a, and Σ37c. Among them, some GB segments are selected for the resistivity measurements. The GB characteristics of each segment are evaluated by scanning electron microscope (SEM) and EBSD analysis of its adjacent grains (Figure 2d) as described in the Methods section. Both are key methods in local characterization of nanostructures and GB segments.[40−42]

The selected GB segments are isolated from their surrounding material by focused ion beam (FIB) milling of two trenches across the film to create a conduction line that includes the GB. Inside the SEM, four needles with 50 nm tip radius probe the FIB-milled structures by forming electrical contacts across the GB as shown in Figure 3. The position of the needles is accurately controlled by piezo-driven micromanipulators. Current is applied through the outer needles

https://doi.org/10.1021/acsnano.1c06367
ACS Nano 2021, 15, 16607−16615

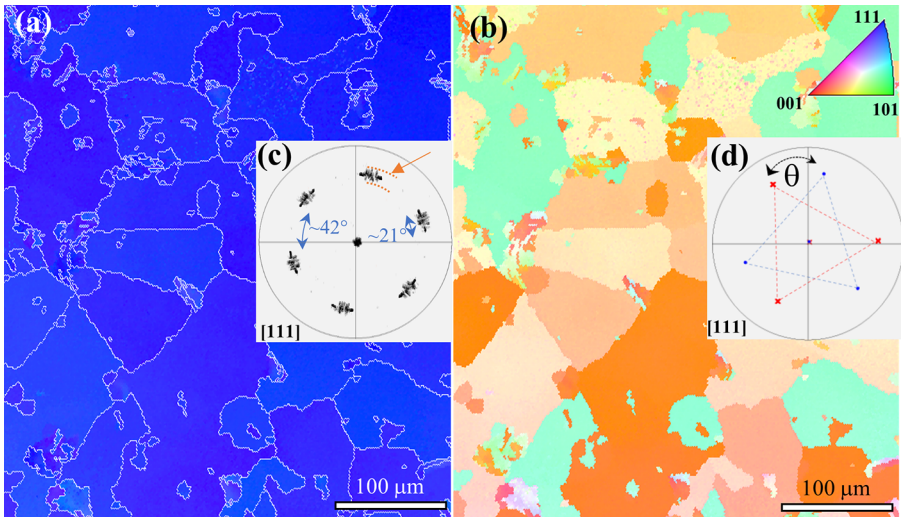

Figure 2. [111] inverse pole figure EBSD-resolved map for (a) out-of-plane and (b) in-plane orientations of the annealed Cu thin films. The maps indicate abnormal grain growth and preferred crystallographic orientations. (c) Pole figure showing a range of [111] tilt grain boundary misorientation. The radial width of the reflection is the maximum spread of twist (orange mark) (d). Pole figure of a selected bicrystal utilized to identify the tilt and twist component of the GB.

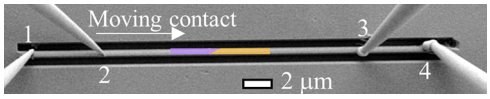

Figure 3. Electrical measurements across a GB. Current is supplied by needles 1 and 4, voltage is measured through needles 2 and 3. All needles are fixed at constant position except needle 2, which scans across the boundary. The EBSD-resolved grain map is laid on top of the GB region. (The tips of needles 3 and 4 are reshaped after electrostatic decharging while positioning them inside the SEM.).

(marked by #1 and #4 in Figure 3), while voltage is measured between the inner needles (marked by #2 and #3 in Figure 3), which are separated by distance L. The resistance R for a conduction line is given by[23]

$$R = \frac{L}{A_{\text{line}}}\rho + \frac{\gamma}{A_{\text{GB}}} \tag{1}$$

where the first term is the contribution of the grain interior with bulk resistivity ρ. The second term is the GB contribution to resistance through GB resistivity γ. This term affects the resistance only when the voltage drop is measured across the GB. A_{line} and A_{GB} represent the cross sections of the conduction line and GB. The measurement technique and its reliability, as well as the use of eq 1 to extract GB resistivity are described in detail in ref 23.

Dependence of GB Resistivity on CSL. GBs with different misorientations were isolated and electrically measured. The GB resistivity dependence on the tilt misorientation (Figure 4) exhibits two regimes; LAGBs where the resistivity increases with the tilt angle, and high angle regime which shows smaller resistivity with larger tilt angle. It suggests that the scattering potential barrier of a GB correlates with its CSL type, while the barrier is only slightly affected by the GB structural characteristics within the same Σ-type. The range of GB resistivity (vertical length of the colored rectangles) covers the spread from all measured segments within the same CSL type, as well as the error bars obtained from 2−3 repeating electrical measurements on the same GB

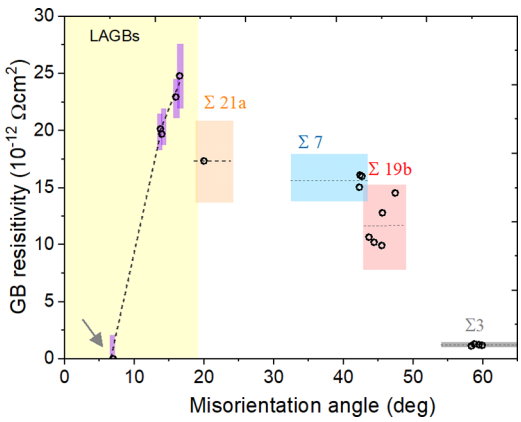

Figure 4. GB resistivities of different CSL GBs and LAGBs. The colored regions represent the spread of the measured values. In the vertical direction, they include the resistance measurement deviation obtained from all measurements within the same CSL type (including different GB structural characteristics). In the horizontal direction, they represent the angular tolerance of CSL type set by the Brandon criterion. The dashed line indicates the average value of resistivity for each CSL type. The resistivity of a 7° LAGB (marked with an arrow) is below the sensitivity of the measurement method.

segment. Multiple segments of the same Σ-type boundary are distinguished by structural variations, which do not noticeably affect resistivity.

Theories on GB resistivities, for example, Mayadas−Shatzkes theory and its extensions,[13,43] relate the strength of the scattering potential at the boundary to the loss of atomic periodicity of the crystal and a change in Fermi velocity of electrons propagating in different directions. However, these models do not supply further information on the effect of characteristics of the material and the boundary (e.g., GB misorientation or motif/phase) on resistivity. On the other hand, DFT calculations predicted that GB resistivity values are a function of the interface excess energy E_{gb}.[14] Indeed, from a structural point of view, quantification of the altered atomic structure at the boundary compared to the grain interior is

https://doi.org/10.1021/acsnano.1c06367
ACS Nano 2021, 15, 16607−16615

made through interface excess properties, for example, interface excess energy (E_{gb}) and excess volume (ΔV). Therefore, we assume that E_{gb} and ΔV represent the deviation of a GB from the background crystalline potential. An increase in excess properties leads to an increase in the fluctuating atomic potential of a GB relative to the bulk, and consequently, a higher scattering potential.[13,17]

To explore such a correlation between GB resistivity and its excess properties, we searched for GB structures with MD annealing simulations using an embedded atom method (EAM) potential[44] that has been successful in reproducing experimental GB structures.[28,31] For each of Σ21a, Σ7, Σ19b, and Σ3, we used both possible symmetric GB planes. The resulting structures are shown in Supporting Information (SI) Figure S1 and the excess properties are plotted in Figure 5a. In case of Σ21a {123}, two structures are observed, one of which resembled a dense dislocation structure with relatively disordered cores. The atomic structure of Σ21a {145} GB clearly consists of a dislocation array and resembles an LAGB.

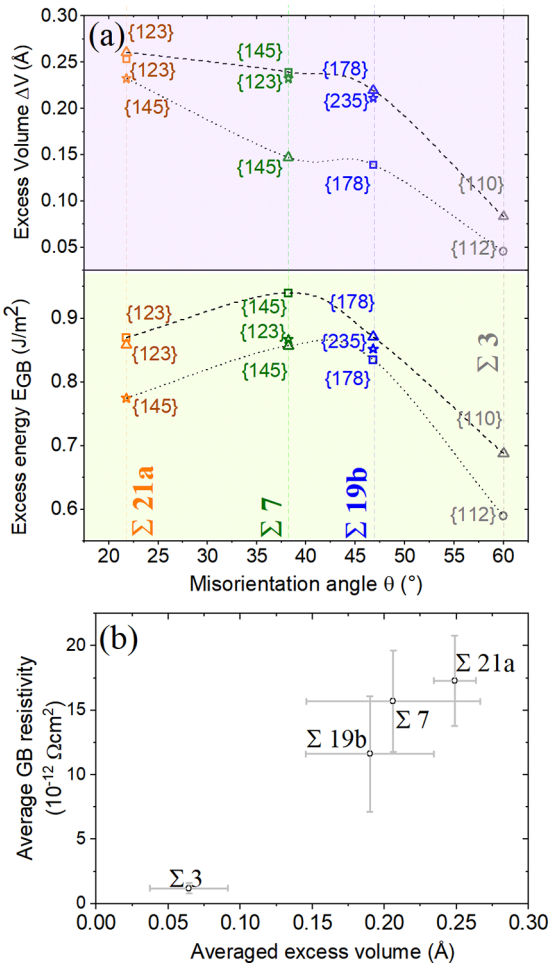

Figure 5. (a) Excess volume and excess energies for several GB phases as calculated using MD simulations. Dashed and dotted lines connect the higher and lower excess values for each CSL type, as a guide for eyes. Each point corresponds to the indicated GB planes, which in some of the cases have multiple possible phases. (b) Correlation between average GB resistivity and averaged excess volume for Cu CSL GBs. The error bars in horizontal direction cover the range of excess volumes of the different GB phases and correspond to Figure 4 in vertical direction.

For Σ19b {178}, we also included the metastable "domino" structure, which was found to occur in experiment.[31] The structure of Σ19b {235} matches to earlier experimental work.[33] The Σ3 {110} data is included, but it should be noted that this GB is prone to faceting, as also observed in earlier simulations.[45,46] While these structures do not represent the complete multitude of asymmetric and defective GB segments which are present in the experimental samples, we can use this data to evaluate general correlations between excess properties and resistivity.

A comparison between GB resistivities and GB excess properties (Figures 4 and 5), which were calculated based on the method shown in ref 47, leads to two main observations. First, resistivity is approximately proportional to the excess volume (Figure 5b), even when considering the substantial variation of ΔV between different GB phases for the same CSL type. The correlation with E_{gb} is weaker, with Σ21a having a lower excess energy, but higher excess volume than the other inspected GBs. This can be explained by its partial LAGB character as deduced from our simulations. Second, there is no obvious correlation between excess properties and resistivity within a specific Σ-type GB, because the excess volume significantly changes within the same CSL type. For example, Figure 5 shows that the differences in E_{gb} and ΔV of the Σ19b GB phases can be larger than the differences of the average values of Σ19b and Σ7 GBs. However, such a difference is not reflected in the resistivity, as seen in Figure 4. This means that the excess volume/resistivity relation is a first order approximation. Secondary effects related to the electronic properties at the boundary, for example, density of states and charge distribution, might also alter the resistivity.[5,15] However, the electronic relations require a separate study, as the current work focuses on the structural effects. In other words, despite E_{gb} and ΔV being clearly connected to GB resistivity across a set of misorientation angles (Figure 5b), the effects of structure for a given Σ value are weak or dominated by defects in the experimental GBs, which will be discussed in more detail in a subsequent section. One should keep in mind that two phases can appear simultaneously within the same GB segment and consequently most of the electrical current would go through the less resistive phase with corresponding lower ΔV. Nevertheless, it is worth noting that the reproducibility of the scattering potential for the selected GBs provides confidence for designing and engineering GBs with predictable resistivities.

Resistivity of Low Angle GBs. The distinct structure of LAGBs from the CSL GBs necessitates a different approach to understand the angular misorientation dependence of GB resistivity. While the high-angle CSL GBs consist of atomistic motifs as repeating units, LAGBs with misorientation θ consist of an array of dislocations aligned along the boundary, separated by a distance $d = (b/2)\cdot\sin(\theta/2)$, where b is the Burgers vector. The resistivity of LAGBs with $\theta = 7°$ ($\pm 1°$) is below the detection limit of the experimental setup. However, an increasing misorientation angle is accompanied by a pronounced monotonic resistivity increment to values which exceed high angle GBs resistivities, as reported in Figure 4. Resistivities of LABGs with more than 10° misorientation are the highest among the measured values, in agreement with earlier predictions that were based on the densities of dislocation arrays.[11]

To understand the resistivity−misorientation angle relation in LAGBs, the dislocation periodicity is examined. Dislocations

https://doi.org/10.1021/acsnano.1c06367
ACS Nano 2021, 15, 16607−16615

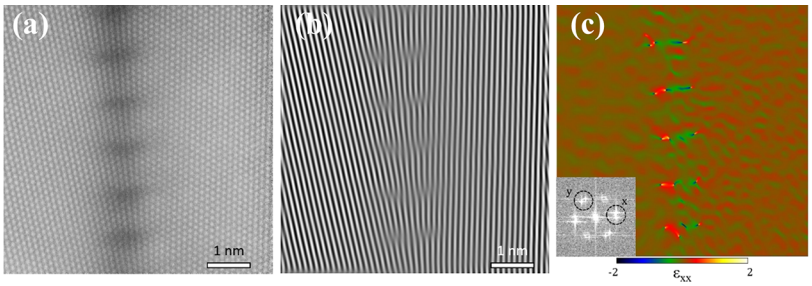

Figure 6. Dislocation array at the 14° LAGB. (a) STEM-HAADF image of the grain boundary. (b) Fast Fourier transform (FFT)-filtered image of (a). Only (111) lattice fringes are shown to visualize the extra half planes. (c) Strain map in the dislocation array analyzed by GPA. FFT in the inset shows the defined direction of the strain. There is a strong strain field at the grain boundary, especially near the core of the partial dislocations.

within the 7° LAGB are expected to have a spacing of ∼2.1 nm under the assumption that the Burgers vector is of 1/2 < 110> type as in face-centered cubic dislocations.[48] The line density of dislocations created by the 7° misorientation does not noticeably affect resistivity as shown in Figure 4. However, an increase in the misorientation to 14° and 18° LAGBs yields a shorter interdislocation distance of 1.05 and 0.82 nm, according to the LAGB Read−Shockley model.[49] STEM high-angle annular dark field (HAADF) images of the 14° boundary show that edge dislocations are aligned along the grain boundary with a separation distance of ∼1 nm (Figure 6), which matches well with the aforementioned calculation. From the strain map calculated by geometrical phase analysis (GPA) and fast Fourier transformation analysis, it is found that the 1/2 < 110> dislocations dissociate into two 1/6 < 211> partials, as observed in ref 48. The dislocation dissociation is clearly observed through the additional half-planes visualized by the (220) lattice reflections. The distance between a set of partial dislocations is comparable to the distance calculated with the Read−Shockley model for full dislocations. This creates a severely strained dislocation array (Figure 6c), in agreement with the deviation from linear elasticity of the Read−Shockley equation for the higher-angle LAGBs.[49] Therefore, the high resistivities of the 14° and 18° GBs are attributed to the highly dense dislocation arrays as well as to the dislocation-induced stress (and strain) field.[49] It should be noted that the LAGB strain field analysis is not considered in the analysis of CSL GBs, since the atomic distortions in the latter type are already covered by the calculated excess volume. Although the GB with 18° misorientation was not characterized by TEM, its electrical behavior suggests that it follows the LAGB behavior and consists of an array of dislocations.[49] A further increase in misorientation to ∼21° results in a resistivity drop, that is, the resistivity does not follow the increasing LAGB energy but a relaxed energy of a CSL structure (Σ21a).[24,50]

GB Resistivity within Same CSL. The effect of structural variation (i.e., inclination, twist, GB plane normal) within the same CSL type on the resistivity is investigated. This is also required to ensure that the comparison between the different Σ-type boundaries is reliable. In this context, the electrical resistivities of Σ19b GB segments having structural variations are acquired through direct resistivity measurements (Table 1). From earlier atomic resolved STEM studies, different GB phases are known to exist for Σ19b [111] $(23\bar{5})$ and $(1\bar{8}7)$ GB plane normals as illustrated in Figure 1b−d.[31,33] It is worth noting that the GB planes extrapolated from the EBSD data refer to an approximation of a straight boundary line over 500−800 nm (width of the cut conduction line), that is, they represent an equivalent straight GB with the corresponding average plane normals. The measured resistivity is similar, within the measurement errors, for all the inspected segments, despite the variation in the GB characteristics.

Table 1. Measured Resistivity for Σ19b GBs[a]

GB type	twist component	$\delta\theta$ (deg) ± 0.5	GB planes	GB phase	GB resistivity (10^{-12} Ωcm^2)
Sym.	yes	1.2	$[23\bar{5}]$	zipper	12.8 ± 1.1
Sym.	no	0.8	$[1\bar{8}7]$	pearl/ domino	14.5 ± 3.5
Asym.	no	2.5	$[2\bar{3}\bar{1}]$; $[9\bar{5}4]$	zipper	9.9 ± 1.7
Asym.	yes	2.4	$[10\bar{1}]$; $[4\bar{3}\bar{1}]$	na	10.2 ± 2.5
Asym.	no	3	$[3\bar{1}\bar{4}]$; $[2\bar{1}\bar{1}]$	na	10.4 ± 1.2

[a]The segments are distinguished by symmetry or asymmetry, twist component, GB planes, and deviation from ideal CSL angle. GB phases are based on Refs 31 and 33. Resistivity is not noticeably affected by these variations within the same CSL type.

The similar resistivities for the different Σ19b GB segments imply that the scattering potential of a boundary does not noticeably change within the same CSL GB type. While it is possible that the different GB phases simply have very similar resistivities, it is more likely that the average GB resistivity is a result of the imperfect GB structures in real materials, which over distances of several hundred nanometres contain multiple deviations from the ideal GB motifs to compensate for local twist components and inclination changes. For instance, the symmetric GB segments (Table 1) with zipper and pearl/domino structures (Figure 1b−d) exhibit similar resistivity, whereas both similarly deviate from an ideal CSL condition. This can explain the unchanged resistivity values for the asymmetric GB segments, since they tend to decompose into symmetric facets and steps in the case of the zipper structure, whereas for the pearl structure, additional subunits are incorporated to compensate for the asymmetric inclinations according to previous TEM studies.[33] Such decomposition definitely creates variations in the atomic structure having a higher scattering potential than the ideal GB unit. Additionally, variations in the GB character, such as a 3° twist component and inclination, still result in similar resistivity values.

Apart from a periodic atomic ordering, a GB consists of defects such as disconnections and dislocations. The defects may appear for several reasons: compensation of GB inclination, asymmetric boundary dissociation, and phase transitions where two phases are separated by a line defect[33,51]

https://doi.org/10.1021/acsnano.1c06367
ACS Nano 2021, 15, 16607−16615

(the macroscopic curvature of the GB does not belong to this group in the current context). Such imperfections do not noticeably change resistivity within a specific CSL tilt GB as indicated by the similar values for the asymmetric and symmetric segments, where the former are expected to contain a higher defect density than the latter, since they can decompose into symmetric segments.[33] Similar results (not presented here) are obtained for the other investigated Σ-types GBs.

Absolute Values of GB Resistivity. The measured resistivities of the GBs ($1-28\cdot10^{-12}$ Ωcm^2) fit the resistivity values obtained by localized electrical measurements of random high angle GBs in Cu thin films ($20-40 \times 10^{-12}$ Ωcm^2) reported by ref 21. However, the values are higher by 1 order of magnitude than the values reported for Cu by macroscopic measurements and predicted by simulations ($0.1-4 \times 10^{-12}$ Ωcm^2).[8,14,16,17,52,53] This might arise from the way GB resistivity values are simulated with DFT, where a relatively low amount of atoms in a defect-free periodic structure is considered, whereas real GB structures are never defect free.[14,16,31,54] Consequently, the calculated values only give lower bounds for the GB resistivity. In addition, our findings also overestimate the resistivity compared to macro-scale experiments. This difference could arise due major limitations of the macroscopic resistivity model, such as not considering GBs aligned along the electric field direction, deviation of scattered electrons from planar wave functions, and varying strengths of potential walls at different GB types. These challenges are comprehensively described in ref 43. In addition, in ref 23, we show that Ga contamination due to FIB milling has a minor effect on the measured resistivity if low milling currents are used. In addition; Cu is not prone to Ga grain boundary segregation due to a high solubility of >10 atom % in bulk Cu. Another factor which can contribute to the high measured resistivity values of GBs is the strain field in the vicinity of the GBs where they attach to the substrate. The strain/stress fields at the triple line of the GB and substrate may cause an additional scattering of electrons.[55] However, this contribution cannot be separated at this stage and should be small as it affects only a small portion of the film thickness.

Despite the high absolute resistivity values measured in this experiment compared to literature, it is still possible to compare relative resistivities of GB types based on predictions. The lack of DFT simulations on resistivities of the investigated GBs, except for Σ3,[14,16,54] prevents us from a direct comparison between our experimental findings and theoretical predictions. Our measured resistivity values of incoherent Σ3 GBs (Figure 4) are higher by almost an order of magnitude than the simulated values for a coherent boundary, 1.06×10^{-12} vs 0.2×10^{-12} Ωcm^2. This difference may be attributed to the different coherency of the GB, where the former is measured for incoherent boundary and the latter calculated for a coherent GB. Calculations predict that high-angle coherent and symmetric CSL GBs have a 10−20 times higher resistance than the coherent Σ3 twin boundary depending on the GB type.[14,16] This result matches our experiments, as the resistivity of high-angle CSL GBs is more than an order of magnitude higher than the resistivity of Σ3 GBs (Figure 4). A similar comparison also applies to LAGB resistivities, where the resistivity values are negligible in the low-angle range, but more pronounced with increasing misorientation angle.[11]

Effect of GB Curvature. GBs usually tend to curve instead of following a straight line, especially for the nanograins (nanocrystals) found in confined integrated circuits. So, understanding the effect of the boundaries' curvature on resistivity is of high significance. To inspect this effect, macroscopically straight and macroscopically curved GB segments are isolated as shown in Figure 7a and Figure 7b,

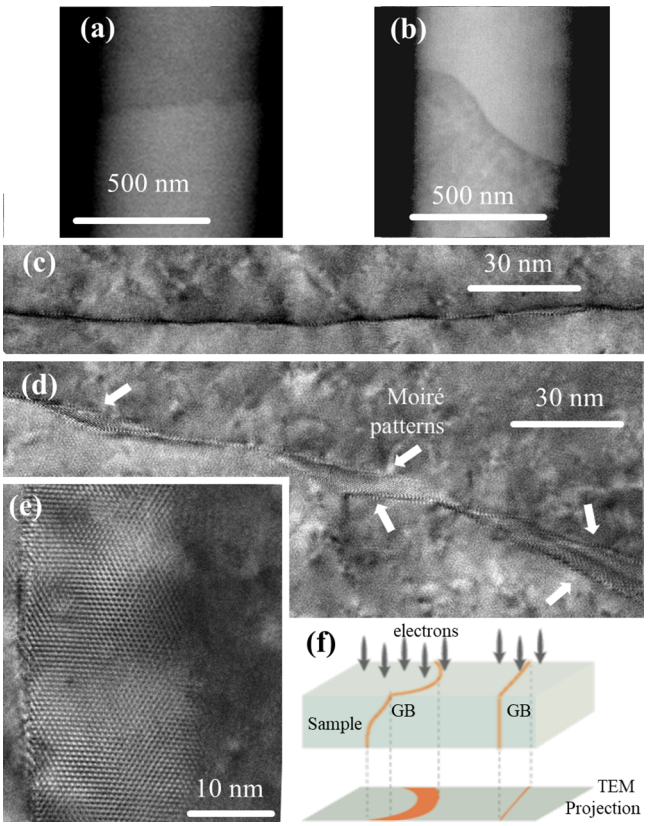

Figure 7. Top view SEM images using BSE detector for (a) straight and (b) curved 14° LAGBs. Top-view high-resolution TEM aberration corrected images of (c) the straight and (d) the curved GBs showing Moiré fringes for the curved GB segment. (e) Higher magnification of the Moiré pattern observed for the curved GB segments, revealing an inclination along the TEM imaging direction. (f) Illustration of the TEM projection for straight and laterally curved boundaries.

respectively. The straight GB segments are described by a pair of GB planes (or a single GB plane for the symmetric GBs) for all the GBs discussed in Figure 4 and Table 1. However, curved GB segments cannot be described in this way, due to the changing inclination along the curve. A significant increase in GB resistivity is observed for GBs with macroscopic in-plane curvature relative to macroscopically straight GB segments. Specifically, curved GBs with misorientations of 14° and 18° exhibit resistivities of (36.1 ± 6) and $(40.3 \pm 6) \times 10^{-12}$ Ωcm^2, compared to (19.7 ± 1.2) and $(22.9 \pm 1.7) \times 10^{-12}$ Ωcm^2 in straight segments, respectively.

To analyze the structural differences between the straight and curved segments, a 14° misorientation LAGB has been observed by top-view TEM. At an atomic scale, both straight and curved GB segments of this LAGB as observed from edge-on imaging conditions have a similar atomic structure consisting of an array of edge dislocations (Figure 6). Obviously, the GB defect density (e.g., disconnections) in the vicinity of a curved GB area is higher compared to the straight segments. However, it has already been shown that the

https://doi.org/10.1021/acsnano.1c06367
ACS Nano 2021, 15, 16607−16615

defect density does not noticeably alter resistivity (Table 1). Yet, as the GB plane normals do not affect resistivity, then the curve must play a role in setting the GB resistivity. The GB plane within the straight segments is aligned normal to the surface, as witnessed by the sharp appearing boundary projection using a top view TEM image (Figure 7c). However, the GB plane within the curve exhibits several nonuniform inclinations which are evidenced in Figure 7d,e by the Moiré pattern on both sides of the boundary, while the zone axes of both grains remain in the common <111> direction. The curvature spans over hundreds of nanometers and the projected width of the GB increases from 1−2 nm in the straight segment to 25 nm in the curved boundary (Figure 7e). Therefore, the curved GB region is not aligned normal to the surface, and instead it creates local spatial deviations as illustrated in Figure 7f. Consequently, the GB normal planes are not perpendicular to the [111] direction, hence a possible loss of the tilt character of the GB. As a consequence, the resistivity increases by 80%. It must be noted that the increase in GB area leads to an underestimation of the GB resistivity due to the inverse relation between GB resistance and its area (eq 1), so the measured increase in GB resistivity due to curvature is a lower bound.

CONCLUSIONS

In conclusion, this study provides an understanding of the relation between the GB structures and electrical resistivity. The research is based on direct and local resistivity measurements of a variety of [111] tilt submicrometer GB segments in Cu, accompanied by structural characterization by EBSD, TEM, and MD simulations. GB resistivity is confirmed to depend on its CSL type, while it is not considerably affected by GB phases and defects within the same CSL type. The GB resistivity is correlated with the boundary's excess volume and excess energy in first approximation. The resistivities of LAGBs with misorientations of more than 10° are the highest among the tilt GBs, due to the high dislocation density and the resulting strain fields. GB curvature increases resistivity of the boundary due to deviation from tilt condition. Overall, this work provides a systematic experimental study on the impact of GB structure on its electrical properties. The results of this study allow GB engineering with clear implications in several industry sectors such as metal interconnects in microelectronics, thermoelectrics, and photovoltaics, where enhancement of resistivity at GB is a major issue limiting the devices' efficiency.

METHODS

Thin Film Preparation and Structural Characterization. High purity Cu thin films (99.999% pure Cu) were deposited on (0001)-oriented α-Al_2O_3 substrates by magnetron sputtering at room temperature. The deposition was performed with a radio frequency (RF) power supply at 250W, 20 sccm Ar flow, and a background pressure of 0.66 Pa. Deposition time of 45 min yielded a nominally 600 nm thick film. Postdeposition thermal annealing was carried out at 400 °C for 2 h within the sputtering chamber without breaking the vacuum. EBSD (EDAX detector in Zeiss Auriga SEM) analysis was employed to identify the crystallographic orientation of grains, as well as GB planes and type (OIM software). Subsequently, selected segments within individual GBs were selected based on the SEM-EBSD results and isolated for further investigation. The selected GB types are tilt GBs: Σ3, Σ7, Σ19b, Σ21a, Σ31a, Σ43b, and low angle GBs with $\theta = 7°$. The selected GB segments for each CSL type consist of different GB planes, deviations from ideal CSL angle and GBs with twist component. SI Table S1 shows the investigated GB segments. In addition, both macroscopically straight and curved segments were investigated.

The GB characteristics of each segment are evaluated by SEM-EBSD with an angular resolution of 0.5° and a step size of 30 nm. The reflections in the (111) pole figures from the adjacent grains yield their misorientation angle $\theta = (\theta_{CSL} + \delta\theta)$ and consequently determines the CSL type (see, e.g., red and blue marks in Figure 2d). The pole figures are also utilized for identifying the GB planes, using a suitable stereographic projection. The inverse pole figure plot readily reveals a possible out-of-plane misalignment of grains. GBs are confirmed to be aligned vertical to surface, with maximum inclination of 3°, as shown in ref 23.

Grain Boundary Segment Fabrication and Electrical Measurements. Electrical investigation of the chosen GB segments is detailed elsewhere.[23] Briefly, each GB segment was isolated from its surrounding film by milling trenches along the whole films' depth. The 30 μm long and ∼0.5 μm wide trenches were created by focused ion beam (FIB-Zeiss Auriga) employing a beam current of 50 pA. *In situ* SEM electrical characterization was conducted utilizing four probes provided by four needles having 50 nm tip radius, which are driven by four independent micromanipulators (Kleindiek − PS4). The resistivity measurements were done utilizing the direct current (dc) pulse method, with 5 mA pulse height and 10 ms pulse width.

Molecular Dynamics Simulations. MD simulations were performed with an embedded atom method (EAM) potential for copper[44] using LAMMPS.[56] First, grain boundaries were assembled from two appropriately oriented crystallites with the ⟨111⟩ tilt axis in z direction and the GB normal in y direction. The bicrystals had a size of approximately 30 × 20 × 6 nm^3 (corresponding to around 300 000−400 000 atoms) with periodic boundaries in z direction and open boundaries otherwise. The open boundaries in contact with the GBs serve as reservoirs for interstitials and vacancies to allow diffusion-driven GB phase transformations.[26] These systems were annealed at 800 K for 4 ns and subsequently cooled to 300 K with a barostat at 0 Pa applied in z direction and an integration time step of 2 fs. Unit cells of the GB phases were cut from these samples, made into cells with periodic boundaries in x and z direction, and scaled to fit the 0 K fcc lattice constant of the copper potential (3.615 Å). Atomic positions were then minimized with regard to the potential energy. The excess properties were calculated from these samples.[47] The structures were visualized with Ovito.[57]

TEM. Atomic structure of the GBs was analyzed using aberration-corrected TEM and STEM, both operated at 300 kV (Titan Themis 60−300, Thermo Fisher Scientific). TEM samples were prepared by using site-specific plane-view lift-out method using a FIB-SEM dual beam workstation (Scios 2, Thermo Fisher Scientific). A 30 kV Ga ion beam was used for the cutting and rough milling and a 5 kV with 48 pA beam was used for the fine milling and cleaning. The probe current of 80 pA was used for high-resolution STEM HAADF imaging with a collection angle of 78−200 mrad and the convergence angle was 23.8 mrad. To minimize scan noise and specimen drift during the acquisition, rigid registration was applied averaging 10 frames recorded with dwell time of 1 μs. Strain distribution at the GB was calculated using GPA, which calculates relative changes in the lattice spacing based on FFT. The strain map in Figure 6c is based on the reflections marked in the FFT in the inset

ASSOCIATED CONTENT

Supporting Information

The Supporting Information is available free of charge at https://pubs.acs.org/doi/10.1021/acsnano.1c06367.

(i) A table of the GB plane normals of the inspected GB segments and (ii) Σ21a, Σ7, Σ19b, Σ3 GB atomic structures (phases) as simulated by MD. Multiple phases are given for each GB type (PDF)

https://doi.org/10.1021/acsnano.1c06367
ACS Nano 2021, 15, 16607−16615

AUTHOR INFORMATION

Corresponding Authors

Hanna Bishara − *Max-Planck-Institut für Eisenforschung GmbH, 40237 Düsseldorf, Germany;* orcid.org/0000-0002-1353-7742; Email: h.bishara@mpie.de

Gerhard Dehm − *Max-Planck-Institut für Eisenforschung GmbH, 40237 Düsseldorf, Germany*; Email: g.dehm@mpie.de

Authors

Subin Lee − *Max-Planck-Institut für Eisenforschung GmbH, 40237 Düsseldorf, Germany; Institute for Applied Materials (IAM), Karlsruhe Institute of Technology, 76344 Eggenstein-Leopoldshafen, Germany;* orcid.org/0000-0002-4629-8004

Tobias Brink − *Max-Planck-Institut für Eisenforschung GmbH, 40237 Düsseldorf, Germany*

Matteo Ghidelli − *Max-Planck-Institut für Eisenforschung GmbH, 40237 Düsseldorf, Germany; Laboratoire des Sciences des Procédés et des Matériaux (LSPM), CNRS, Université Sorbonne Paris Nord, 93430 Villetaneuse, France;* orcid.org/0000-0001-6057-9040

Complete contact information is available at: https://pubs.acs.org/10.1021/acsnano.1c06367

Funding

Open access funded by Max Planck Society.

Notes

The authors declare no competing financial interest.

ACKNOWLEDGMENTS

H.B., T.B., and G.D. acknowledge the financial support by the ERC Advanced Grant GB CORRELATE (Grant Agreement 787446 GB-CORRELATE). S.L. acknowledges the financial support by Alexander von Humboldt Foundation.

REFERENCES

(1) Pan, C.; Naeemi, A. A Proposal for a Novel Hybrid Interconnect Technology for the End of Roadmap. *IEEE Electron Device Lett.* **2014**, *35* (2), 250−252.

(2) Graham, R. L.; Alers, G. B.; Mountsier, T.; Shamma, N.; Dhuey, S.; Cabrini, S.; Geiss, R. H.; Read, D. T.; Peddeti, S. Resistivity Dominated by Surface Scattering in Sub-50 Nm Cu Wires. *Appl. Phys. Lett.* **2010**, *96* (4), 42116.

(3) Barmak, K.; Darbal, A.; Ganesh, K. J.; Ferreira, P. J.; Rickman, J. M.; Sun, T.; Yao, B.; Warren, A. P.; Coffey, K. R. Surface and Grain Boundary Scattering in Nanometric Cu Thin Films: A Quantitative Analysis Including Twin Boundaries. *J. Vac. Sci. Technol., A* **2014**, *32* (6), 61503.

(4) Barmak, K.; Ezzat, S.; Gusley, R.; Jog, A.; Kerdsongpanya, S.; Khaniya, A.; Milosevic, E.; Richardson, W.; Sentosun, K.; Zangiabadi, A.; Gall, D.; Kaden, W. E.; Mucciolo, E. R.; Schelling, P. K.; West, A. C.; Coffey, K. R. Epitaxial Metals for Interconnects beyond Cu. *J. Vac. Sci. Technol., A* **2020**, *38* (3), 33406.

(5) Gall, D. The Search for the Most Conductive Metal for Narrow Interconnect Lines. *J. Appl. Phys.* **2020**, *127* (5), 50901.

(6) Qiu, Q.; Liu, Y.; Xia, K.; Fang, T.; Yu, J.; Zhao, X.; Zhu, T. Grain Boundary Scattering of Charge Transport in *n-type* (Hf,Zr)CoSb Half-Heusler Thermoelectric Materials. *Adv. Energy Mater.* **2019**, *9* (11), 1803447.

(7) Muzzillo, C. P. Review of Grain Interior, Grain Boundary, and Interface Effects of K in CIGS Solar Cells: Mechanisms for Performance Enhancement. *Sol. Energy Mater. Sol. Cells* **2017**, *172*, 18−24.

(8) Lu, L.; Shen, Y.; Chen, X.; Qian, L.; Lu, K. Ultrahigh Strength and High Electrical Conductivity in Copper. *Science (Washington, DC, U. S.)* **2004**, *304* (5669), 422 LP−426.

(9) Gomell, L.; Roscher, M.; Bishara, H.; Jägle, E. A.; Scheu, C.; Gault, B. Properties and Influence of Microstructure and Crystal Defects in Fe2VAl Modified by Laser Surface Remelting. *Scr. Mater.* **2021**, *193*, 153−157.

(10) Yang, Y. M.; Yu, A.; Hsu, B.; Hsu, W. C.; Yang, A.; Lan, C. W. Development of High-Performance Multicrystalline Silicon for Photovoltaic Industry. *Prog. Photovoltaics* **2015**, *23* (3), 340−351.

(11) Lormand, G. Electrical Properties of Grain Boundaries. *J. Phys. Colloq.* **1982**, *43* (C6), C6−283.

(12) Feldman, B.; Park, S.; Haverty, M.; Shankar, S.; Dunham, S. T. Simulation of Grain Boundary Effects on Electronic Transport in Metals, and Detailed Causes of Scattering. *Phys. Status Solidi B* **2010**, *247* (7), 1791−1796.

(13) Mayadas, A. F.; Shatzkes, M. Electrical-Resistivity Model for Polycrystalline Films: The Case of Arbitrary Reflection at External Surfaces. *Phys. Rev. B* **1970**, *1* (4), 1382−1389.

(14) César, M.; Liu, D.; Gall, D.; Guo, H. Calculated Resistances of Single Grain Boundaries in Copper. *Phys. Rev. Appl.* **2014**, *2* (4), 44007.

(15) César, M.; Gall, D.; Guo, H. Reducing Grain-Boundary Resistivity of Copper Nanowires by Doping. *Phys. Rev. Appl.* **2016**, *5* (5), 54018.

(16) Lanzillo, N. A. *Ab initio* Evaluation of Electron Transport Properties of Pt, Rh, Ir, and Pd Nanowires for Advanced Interconnect Applications. *J. Appl. Phys.* **2017**, *121* (17), 175104.

(17) Bakonyi, I. Accounting for the Resistivity Contribution of Grain Boundaries in Metals: Critical Analysis of Reported Experimental and Theoretical Data for Ni and Cu. *Eur. Phys. J. Plus* **2021**, *136* (4), 410.

(18) Bakonyi, I.; Isnaini, V. A.; Kolonits, T.; Czigány, Z.; Gubicza, J.; Varga, L. K.; Tóth-Kádár, E.; Pogány, L.; Péter, L.; Ebert, H. The Specific Grain-Boundary Electrical Resistivity of Ni. *Philos. Mag.* **2019**, *99* (9), 1139−1162.

(19) Nakamichi, I. Electrical Resistivity and Grain Boundaries in Metals. *Mater. Sci. Forum* **1996**, *207−209*, 47−58.

(20) Steinhögl, W.; Schindler, G.; Steinlesberger, G.; Traving, M.; Engelhardt, M. Comprehensive Study of the Resistivity of Copper Wires with Lateral Dimensions of 100 Nm and Smaller. *J. Appl. Phys.* **2005**, *97* (2), 23706.

(21) Kim, T.-H.; Zhang, X.-G.; Nicholson, D. M.; Evans, B. M.; Kulkarni, N. S.; Radhakrishnan, B.; Kenik, E. A.; Li, A.-P. Large Discrete Resistance Jump at Grain Boundary in Copper Nanowire. *Nano Lett.* **2010**, *10* (8), 3096−3100.

(22) Kitaoka, Y.; Tono, T.; Yoshimoto, S.; Hirahara, T.; Hasegawa, S.; Ohba, T. Direct Detection of Grain Boundary Scattering in Damascene Cu Wires by Nanoscale Four-Point Probe Resistance Measurements. *Appl. Phys. Lett.* **2009**, *95* (5), 52110.

(23) Bishara, H.; Ghidelli, M.; Dehm, G. Approaches to Measure the Resistivity of Grain Boundaries in Metals with High Sensitivity and Spatial Resolution: A Case Study Employing Cu. *ACS Appl. Electron. Mater.* **2020**, *2* (7), 2049−2056.

(24) Frost, H. J.; Ashby, M.F; Spaepen, F A Catalogue of [100], [110], and [111] Symmetric Tilt Boundaries in Face-Centered Cubic Hard Sphere Crystals. Mater. Res. Lab. Tech. Rep. (National Sci. Found. Grant DMR 80−20247). Cambridge, MA *Harvard Div. Appl. Sci.* **1982**, *1*.

(25) Brandon, D. G. The Structure of High-Angle Grain Boundaries. *Acta Metall.* **1966**, *14* (11), 1479−1484.

(26) Frolov, T.; Olmsted, D. L.; Asta, M.; Mishin, Y. Structural Phase Transformations in Metallic Grain Boundaries. *Nat. Commun.* **2013**, *4* (1), 1899.

(27) Zhu, Q.; Samanta, A.; Li, B.; Rudd, R. E.; Frolov, T. Predicting Phase Behavior of Grain Boundaries with Evolutionary Search and Machine Learning. *Nat. Commun.* **2018**, *9* (1), 467.

(28) Peter, N. J.; Frolov, T.; Duarte, M. J.; Hadian, R.; Ophus, C.; Kirchlechner, C.; Liebscher, C. H.; Dehm, G. Segregation-Induced

Nanofaceting Transition at an Asymmetric Tilt Grain Boundary in Copper. *Phys. Rev. Lett.* **2018**, *121* (25), 255502.
(29) Cahn, W. J. Transitions and Phase Equilibria Among Grain Boundary Structures. *J. Phys. Colloq.* **1982**, *43* (C6), C6−199−C6−213.
(30) Rottman, C. Theory of Phase Transitions at Internal Interfaces. *J. Phys. Colloq.* **1988**, *49* (C5), C5−313−C5−326.
(31) Meiners, T.; Frolov, T.; Rudd, R. E.; Dehm, G.; Liebscher, C. H. Observations of Grain-Boundary Phase Transformations in an Elemental Metal. *Nature* **2020**, *579* (7799), 375−378.
(32) Hart, E. W. Two-Dimensional Phase Transformation in Grain Boundaries. *Scr. Metall.* **1968**, *2* (3), 179−182.
(33) Meiners, T.; Duarte, J. M.; Richter, G.; Dehm, G.; Liebscher, C. H. Tantalum and Zirconium Induced Structural Transitions at Complex [111] Tilt Grain Boundaries in Copper. *Acta Mater.* **2020**, *190*, 93−104.
(34) Dehm, G.; Rühle, M.; Ding, G.; Raj, R. Growth and Structure of Copper Thin Films Deposited on (0001) Sapphire by Molecular Beam Epitaxy. *Philos. Mag. B* **1995**, *71* (6), 1111−1124.
(35) Dehm, G.; Edongué, H.; Wagner, T.; Oh, S.; Arzt, E. Obtaining Different Orientation Relationships for Cu Films Grown on (0001) α-Al2O3 Substrates by Magnetron Sputtering. *Z. Metallkd.* **2005**, *96*, 249−254.
(36) Oh, S. H.; Scheu, C.; Wagner, T.; Rühle, M. Control of Bonding and Epitaxy at Copper/Sapphire Interface. *Appl. Phys. Lett.* **2007**, *91* (14), 141912.
(37) Barmak, K.; Eggeling, E.; Sharp, R.; Roberts, S.; Shyu, T.; Sun, T.; Yao, B.; Ta'asan, S.; Kinderlehrer, D.; Rollett, A. D.; Coffey, K. Grain Growth and the Puzzle of Its Stagnation in Thin Films a Detailed Comparison of Experiments and Simulations. *Mater. Sci. Forum* **2012**, *715−716*, 473−479.
(38) Glushko, O.; Dehm, G. Initiation and Stagnation of Room Temperature Grain Coarsening in Cyclically Strained Gold Films. *Acta Mater.* **2019**, *169*, 99−108.
(39) Wynblatt, P.; Chatain, D. Importance of Interfacial Step Alignment in Hetero-Epitaxy and Orientation Relationships: The Case of Ag Equilibrated on Ni Substrates. Part 1 Computer Simulations. *J. Mater. Sci.* **2015**, *50* (15), 5262−5275.
(40) An, D.; Griffiths, T. A.; Konijnenberg, P.; Mandal, S.; Wang, Z.; Zaefferer, S. Correlating the Five Parameter Grain Boundary Character Distribution and the Intergranular Corrosion Behaviour of a Stainless Steel Using 3D Orientation Microscopy Based on Mechanical Polishing Serial Sectioning. *Acta Mater.* **2018**, *156*, 297−309.
(41) Natarajan, P.; Shalabny, A.; Sadhujan, S.; Idilbi, A.; Bashouti, M. Y. The Non-Stationary Case of the Maxwell-Garnett Theory: Growth of Nanomaterials (2D Gold Flakes) in Solution. *Nanoscale Adv.* **2020**, *2* (3), 1066−1073.
(42) Hoffmann, B.; Bashouti, M. Y.; Feichtner, T.; Mačković, M.; Dieker, C.; Salaheldin, A. M.; Richter, P.; Gordan, O. D.; Zahn, D. R. T.; Spiecker, E.; Christiansen, S. New Insights into Colloidal Gold Flakes: Structural Investigation, Micro-Ellipsometry and Thinning Procedure towards Ultrathin Monocrystalline Layers. *Nanoscale* **2016**, *8* (8), 4529−4536.
(43) Munoz, R. C.; Arenas, C. Size Effects and Charge Transport in Metals: Quantum Theory of the Resistivity of Nanometric Metallic Structures Arising from Electron Scattering by Grain Boundaries and by Rough Surfaces. *Appl. Phys. Rev.* **2017**, *4* (1), 11102.
(44) Mishin, Y.; Mehl, M. J.; Papaconstantopoulos, D. A.; Voter, A. F.; Kress, J. D. Structural Stability and Lattice Defects in Copper: *Ab initio*, Tight-Binding, and Embedded-Atom Calculations. *Phys. Rev. B: Condens. Matter Mater. Phys.* **2001**, *63* (22), 224106.
(45) Wu, Z. X.; Zhang, Y. W.; Srolovitz, D. J. Grain Boundary Finite Length Faceting. *Acta Mater.* **2009**, *57* (14), 4278−4287.
(46) Wang, J.; Li, N.; Misra, A. Structure and Stability of Σ3 Grain Boundaries in Face Centered Cubic Metals. *Philos. Mag.* **2013**, *93* (4), 315−327.
(47) Frolov, T.; Mishin, Y. Thermodynamics of Coherent Interfaces under Mechanical Stresses. II. Application to Atomistic Simulation of Grain Boundaries. *Phys. Rev. B: Condens. Matter Mater. Phys.* **2012**, *85* (22), 224107.
(48) Zhang, X.; Han, J.; Plombon, J. J.; Sutton, A. P.; Srolovitz, D. J.; Boland, J. J. Nanocrystalline Copper Films Are Never Flat. *Science (Washington, DC, U. S.)* **2017**, *357* (6349), 397 LP−400.
(49) Hull, D.; Bacon, D. J. Chapter 9 - Dislocation Arrays and Crystal Boundaries. In *Introduction to Dislocations*, 5th ed.; Butterworth-Heinemann: Oxford, 2011; pp 171−204; DOI: 10.1016/B978-0-08-096672-4.00009-8.
(50) Parajuli, P.; Romeu, D.; Hounkpati, V.; Mendoza-Cruz, R.; Chen, J.; Yacamán, M. J.; Flowers, J.; Ponce, A. Misorientation Dependence Grain Boundary Complexions in < 111> Symmetric Tilt Al Grain Boundaries. *Acta Mater.* **2019**, *181*, 216−227.
(51) Hirth, J. P.; Pond, R. C. Steps, Dislocations and Disconnections as Interface Defects Relating to Structure and Phase Transformations. *Acta Mater.* **1996**, *44* (12), 4749−4763.
(52) Andrews, P. V.; West, M. B.; Robeson, C. R. The Effect of Grain Boundaries on the Electrical Resistivity of Polycrystalline Copper and Aluminium. *Philos. Mag.* **1969**, *19* (161), 887−898.
(53) Mannan, K. M.; Karim, K. R. Grain Boundary Contribution to the Electrical Conductivity of Polycrystalline Cu Films. *J. Phys. F: Met. Phys.* **1975**, *5* (9), 1687−1693.
(54) Valencia, D.; Wilson, E.; Jiang, Z.; Valencia-Zapata, G. A.; Wang, K.-C.; Klimeck, G.; Povolotskyi, M. Grain-Boundary Resistance in Copper Interconnects: From an Atomistic Model to a Neural Network. *Phys. Rev. Appl.* **2018**, *9* (4), 44005.
(55) Cordill, M. J.; Glushko, O.; Putz, B. Electro-Mechanical Testing of Conductive Materials Used in Flexible Electronics. *Front. Mater.* **2016**, *3*, 11.
(56) Plimpton, S. Fast Parallel Algorithms for Short-Range Molecular Dynamics. *J. Comput. Phys.* **1995**, *117* (1), 1−19.
(57) Stukowski, A. Visualization and Analysis of Atomistic Simulation Data with OVITO−the Open Visualization Tool. *Modell. Simul. Mater. Sci. Eng.* **2010**, *18* (1), 15012.

https://doi.org/10.1021/acsnano.1c06367
ACS Nano 2021, 15, 16607−16615